ORIGINAL PAPER

Revisiting Wagner's Criteria to Predict Establishment and Retention of Alumina Scales on Ternary NiCrAl Alloys

R. Pillai[1] · C. J. Stephens[2]

Abstract

Despite the advent of numerical modeling approaches and high-performance computing infrastructure, the design and development of corrosion-resistant high temperature alloys (> 500 °C) continue to be largely empirical and typically involve extensive experimentation. This is mainly due to the lack of a single unified physics-based model that can address the impact of multiple competing factors such as time, environment, alloy composition, microstructure, and geometry. The classical Wagner's criteria have been foundational to estimate the minimum concentrations required of an oxide-forming element to establish and sustain a protective oxide scale. However, the formulation is primarily limited to lower-order alloy systems (binary alloys) and ignores the time dependence of subsurface compositional changes in the alloy. The lack of key data on the temperature and composition dependence of the solubility and transport of oxidants in multicomponent-multiphase alloys further exacerbates the problem. In the present work, a few of these limitations were addressed using a flux-based approach (FLAP) which tracks the spatiotemporal evolution of the fundamental flux balance between oxygen and the oxide-forming elements to enable the prediction of the formation of an external alumina scale in ternary NiCrAl alloys. The modeling results were validated with the literature findings and additional experimental work conducted in the present work.

keywords NiCrAl alloys · Transition from internal to external oxidation · Computation-assisted design of oxidation resistant alloys

✉ R. Pillai
   pillairr@ornl.gov

[1] Materials Science and Technology Division, Oak Ridge National Laboratory, Oak Ridge, TN 37831-6156, USA

[2] Advanced High Temperature Materials, University of Virginia, Charlottesville, USA

Introduction

The realization of a carbon–neutral energy landscape relies on the availability of cost-effective high temperature materials with optimum mechanical properties and environmental resistance. Balancing desired long-term structural properties and corrosion resistance while minimizing total material costs is a continuing challenge for alloy developers. High temperature corrosion resistance is usually a critical barrier in the rapid evaluation, development and integration of high-temperature industrial alloys for future power generation and transportation applications [1, 2]. Additionally, corrosive processes may induce microstructural changes in the alloy which may in turn deteriorate the mechanical properties [3, 4]. Experimental evaluation and characterization of candidate structural materials are expensive and time-consuming due to the need to simultaneously consider the impact of the multiple parameters that influence the corrosion behavior of the material such as chemical composition, operating conditions, service environment and component geometry. Significant progress has been made in employing models to predict high temperature corrosion-induced material degradation and lifetimes [5]. A combination of numerical approaches, ever-increasing computing power and evolving thermodynamic/kinetic databases has provided a cost-effective and reliable alternative to purely experimental procedures and provided a better understanding of environmental effects [6–11].

However, looking over the past 70 years of high temperature alloy development specifically with some important examples at Oak Ridge National Laboratory, beginning with the Ni-based alloy Hastelloy-N for molten salt reactors (MSRs) [12], the ferritic–martensitic T91 steel [13] and the alumina-forming austenitic alloys (AFAs) [14], the use of modeling methods for designing corrosion resistant materials has been incremental [15]. Even with computational guidance, the development of AFAs required over 50 lab-scale alloys and 5–10 iterative loops to optimize strengthening phases (mechanical properties) and ensure formation of an external alumina scale (oxidation resistance). Ideally, models capable in aiding design and development of corrosion resistant alloys are expected to predict the following key design criteria as a function of alloy chemistry, atmosphere, component geometry, time and temperature:

- Formation of desired protective external oxide layers
- Growth kinetics of the oxide layers
- Oxide failure rates
- Corrosion-induced compositional changes and phase transformations in the alloy
- Impact of corrosion-induced degradation on lifetime and mechanical properties
- Transport through the oxide layers
- Effect of alloy composition on solubility of oxidants

A thorough review of the state-of-the art in modeling methodologies to address the above goals was given by Pillai et al. [5] and will not be discussed here. The present work will focus on models to predict the formation of protective external scales on high temperature alloys. As discussed in [5], efforts to understand and quantify the effect

of time, temperature, surface chemistry, alloy and gas compositions on the transport mechanisms in the oxide scales are a mammoth task given the sensitivity of oxide scale microstructure on these variables and the lack of composition-dependent thermodynamic and kinetic data for a multicomponent commercial alloys. Fortunately, the classical Wagner's criteria provides a practical approach to predict the minimum concentration of the alloying element (e.g., Cr or Al) required to form the protective oxide (e.g., Cr_2O_3 or Al_2O_3). The critical concentration required to form an external chromia or alumina scale $N^*_{Cr,Al}$ was given by Wagner [16] as,

$$N^*_{Cr,\,Al} = \sqrt{\frac{\pi f^*_{IOZ}}{2\nu} \frac{V_{alloy}}{V_{oxide}} \frac{N^{(s)}_O D_O}{D_{Cr,\,Al}}} \tag{1}$$

where V_{alloy} and V_{oxide} are the molar volumes of the alloy and metal (M) oxide (MO_ν), respectively, $N^{(s)}_O$ is the oxygen solubility in the alloy on the surface, D_O is the diffusion coefficient of O in the alloy, $D_{Cr,\,Al}$ is the interdiffusion coefficient of Cr or Al, and f^*_{IOZ} is the critical volume fraction of internal oxides beyond which an external scale may form. Although extremely useful and successful in various cases, the Wagner's criteria is predominantly limited to binary alloys due to the nature of Eq. (1) and lack of data on the temperature and alloy composition dependence of $N^{(s)}_O$, D_O, $D_{Cr,\,Al}$ and f^*_{IOZ} for multicomponent and multiphase alloys. Furthermore, Eq. (1) does not account for the oxidation-induced and time-dependent compositional changes in the alloy subsurface. Acquiring information on the aforementioned parameters is extremely challenging [17] and attempts to address this shortcoming unfortunately receive limited attention in the current high temperature materials research landscape primarily due to the demanding time-constrained technology readiness levels the models are expected to achieve. Consequently, high temperature corrosion-resistant alloys design continues to be largely empirical.

In the present work, an alternative flux-based approach (abbreviated as FLAP) has been proposed to estimate N^*_{Al} in ternary NiCrAl alloys. It is well established and has been shown in the literature that Eq. (1) fails to predict N^*_{Al} in ternary NiCrAl alloys as it significantly underestimates the minimum Al required in these alloys to form an external Al_2O_3 scale [18], as experimentally determined by Giggins and Pettit [19]. The flux-balance condition between the inward flux of oxygen and the outward flux of Al is the basis of FLAP which eliminates the limitation of binary alloy systems and enables the consideration of spatiotemporal compositional changes and the cross-term interactions in multicomponent and multiphase systems. The input data for the modeling approach are the concentration and temperature dependence of the internal oxidation kinetics in binary NiCr and NiAl alloys. This information was estimated by performing additional simulations for dilute NiCr and NiAl alloy compositions experimentally evaluated by Whittle et al. [20]. The modeling predictions in each case were validated with corresponding experimental results from Whittle et al. [20] and Giggins and Pettit at 1000 °C [19]. Additional validation was performed with experiments conducted in the present work for ternary NiCrAl alloys at 950 °C.

Table 1 Measured composition (Inductively Coupled Plasma Optical Emission spectroscopy) of the ternary NiCrAl alloys for the major elements Ni, Cr and Al studied in the present work in wt.%. The total impurities (C, S, O an N) were less than 70 wppm (parts per million in weight) in all the alloys.

Base NiCr	Ni	Cr	Al
Ni-18Cr-2Al	80.0	18.1	1.9
Ni-18Cr-4Al	78.2	17.9	3.9
Ni-22Cr-1Al	76.1	22.8	1.1
Ni-22Cr-2Al	76.4	21.7	1.9
Ni-22Cr-4Al	74.1	22.0	3.9

Experimental Procedure

Three model austenitic Ni–Cr–Al alloys were inductively melted and cast with pure element feedstock at Oak Ridge National Laboratory. After casting, the material was hot-rolled at 1050 °C down to a thickness of about 8 mm and subsequently annealed at 1050 °C for 1 h in high-purity Ar. Measurement of grain sizes was performed in accordance with the ASTM E112 procedure. Measured dimensions (length and breadth) were converted to equivalent diameters assuming a circular grain. The average grain diameter in the alloys was about 80 μm with a standard deviation of 36 μm. The chemical compositions of the alloys tested in the present work are given in Table 1.

Alloy coupons ($\sim 10 \times 20 \times 1.5$ mm) were ground to a 600-grit finish and ultrasonically cleaned in acetone and methanol prior to exposure. The specimens were isothermally exposed at 950 °C for 8 h and 24 h in a resistively heated alumina tube furnace in flowing dry laboratory air. After the test duration, the samples were slow-cooled in the furnace under the test gas atmosphere. The mass changes were measured using a Mettler-Toledo model XP205 balance with an accuracy of ± 0.04 mg.

After exposure the specimens were Cu electroplated, cross-sectioned and mounted. The mounted samples were polished using SiC papers, diamond pastes (1 micron) and colloidal SiO_2 for cross-sectional characterization including scanning electron microscopy (SEM) using a TESCAN model MIRA3, energy-dispersive X-ray spectroscopy (EDS) using EDAX Octane Elect Super Silicon Drift Detector with an EDS detector (70 mm^2). EDS elemental mapping was performed at 20 kV and quantitatively analyzed using the APEX EDS 3.0 software with the ZAF correction method (Z: atomic number, A: absorbance, F: fluorescence) and in-built standards.

Modeling Procedure

A previously developed coupled thermodynamic-kinetic approach [21] was employed to model the oxygen permeation and the calculations to predict transition from internal to external oxidation. The modified form of the modeling

procedure to allow calculations to be run on parallel computing cores and thereby accelerate the simulations was utilized in the present work [22]. A brief summary of the procedure will be mentioned here.

The procedure begins with the discretization the domain into a suitable number of volume elements or slices of width Δz^i, i being the slice number. The position of the boundaries of these slices is marked as z^j, where $j = i + 1$. The center of the slices is marked as l^i. Average mole fractions N_c^{i0} for each constituent c are assigned to each slice based on the initial composition of the system. Constant molar volume V_m is assumed across the entire specimen. Initial phase fractions f_φ, compositions and chemical potentials μ_c^i in each slice are defined by equilibrium calculations based on local element concentrations, temperature, and pressure. This is followed by choosing a suitable time step Δt for calculating diffusion of elements with the modified flux equation of Larsson et al. [23] in the lattice-fixed frame of reference. Efficient equilibration of vacancies ($\Delta \mu v_A = 0$) was assumed. The flux of each constituent in a slice, J_c^i is evaluated as follows,

$$J_c^i = -\frac{M_c^{i,\mathrm{eff}}}{V_m\left(l^{i+1} - l^i\right)} \sqrt{N_c^{i+1} N_c^i} \, 2 \sinh\left(\frac{\mu_c^{i+1} - \mu_c^i}{2RT}\right) \tag{2}$$

where $M_c^{i,\mathrm{eff}}$ is the effective mobility of constituent c in slice i, μ_c^i is the chemical potential of constituent c at location i, R is the universal gas constant, and T is the temperature. Various alternatives to evaluate the local effective kinetic properties such as mobilities are documented in [24]. In this work, the upper Wiener bounds or more generally termed the "Rule of Mixtures" have been used with the phase fraction $f^\emptyset$ and mobility $M_c^\emptyset$ for the individual phase $\emptyset$ as follows,

$$M_c^{i,\mathrm{eff}} = \sum_{\emptyset=1}^{\emptyset} f^\emptyset M_c^\emptyset \tag{3}$$

Diffusion was considered to occur only in the γ (disordered FCC), γ' (ordered FCC), β-NiAl (ordered BCC) and α-Cr (disordered BCC) phases. Overall, the phases γ-FCC, γ'-FCC, β-BCC, α-Cr and Corundum (Cr_2O_3 and Al_2O_3) were considered for the calculations. Thermodynamic and kinetic data were taken from the databases TCNi11 [25] and MobNi5 [26], respectively. Wherever deemed essential (e.g., cold-worked surfaces, finer grain sizes < 100 μm), the alloy constituent mobilities M_c extracted from the mobility database (MOBNI5) were modified to M_c^{mod} to account for the grain-boundary-assisted diffusion in the following manner:

$$M_c^{\mathrm{mod}} = \frac{\delta}{d} M_c^{\mathrm{GB}} + \left(1 - \frac{\delta}{d}\right) M_c \tag{4}$$

where M_c^{GB} is the mobility of constituent c in grain boundaries, δ is the grain boundary width, and d is the grain size.

Oxygen Permeation Calculations for Binary NiCr and NiAl Alloys

To predict the oxygen permeation in NiCr and NiAl binary alloys, the data for measured oxygen solubility $N_O^{(s)}$ in pure Ni by Park and Altstetter was employed [27]. The oxygen solubility $N_O^{(s)}$ was implemented as a fixed concentration for O on the alloy surface to replicate the high temperature exposures in Ni-NiO Rhines pack conducted by Whittle et al. for the dilute binary NiCr and NiAl alloys [20]. The initial concentrations of Cr and Al in the respective alloys were used to define the initial condition with the O concentration in alloy set to a low value of 1×10^{-6} at. %.

Calculations to Predict Transition from Internal to External Oxidation (FLAP)

It has been shown in numerous publications that the thermodynamic and kinetic databases for Ni-based alloys by Thermo-Calc are adequate and provide reliable predictions on the corrosion-induced compositional changes and phase transformations in multicomponent and multiphase Ni-based alloys, that have been shown to agree with even long-term experimental results (~ 30 kh) [28–33]. Given that precise thermodynamic description of the oxides in multicomponent Ni–Cr–Al–O systems and corresponding kinetic data for O in these alloys as a function of alloy composition is lacking [5], an alternative approach was undertaken to overcome this limitation. This is a necessary step for the method to be extended to even higher-order alloy systems (e.g., commercial alloys with > 4 alloying elements and multiple phases) where there will continue to be a lack of sufficient data on oxygen solubility, diffusion and oxide stabilities.

The calculated concentration and temperature-dependent surface flux of O for the dilute binary NiCr and NiAl alloys were utilized to determine the corresponding fluxes required to form either Cr_2O_3 or Al_2O_3, respectively, in the ternary Ni–Cr–Al alloys as follows,

$$\gamma J_{\text{Cr, Al}} = J_{O\,(Cr_2O_3/Al_2O_3)} \tag{5}$$

where γ is the stoichiometric coefficient for the respective oxides. For exposures in air or in general under O partial pressures above the dissociation pressure for NiO, it was assumed that Ni will initially oxidize followed by Cr and then Al. A strict condition was set to determine whether an external scale will form. If the outward flux of Cr or Al in the second cell of the computational domain (minimum cell size of 2 μm) was greater than the one given by Eq. (5) before the calculated concentration and temperature-dependent depth of internal oxidation equals the distance from the alloy surface, an external scale was assumed to form. Alternatively, the alloy was predicted to internally oxidize. In case the external chromia or alumina scale forms, the Cr\Al consumption was given by the corresponding oxidation kinetics of chromia or alumina at that temperature. If the alloy oxidized internally, the flux of Cr\Al in the internal oxidation zone was set to zero, in accordance with Wagner [16].

It is not sufficient to only predict the likelihood of formation of an external protective scale. The potential to sustain that scale as a function of time and

temperature needs to be additionally evaluated. Wagner [34] derived the following equation to estimate the minimum concentration required at the scale/alloy interface to sustain external scale formation,

$$N_{Cr,\,Al}^* = \frac{V_{alloy}}{V_{oxide}} \sqrt{\frac{\pi k_p}{2D_{Cr,\,Al}}} \tag{6}$$

where V_{alloy} and V_{oxide} are the molar volumes of the alloy and oxide, respectively, and k_p is the parabolic rate constant for the external scale (e.g., Cr_2O_3 or Al_2O_3). As in the case of Eq. (1), Eq. (6) presents a similar limitation as to the lack of consideration of cross-term effects on $D_{Cr,\,Al}$. In the present work, the fundamental flux balance at the oxide–alloy interface which was the basis to derive Eq. (5) has been employed. The flux balance states that if the flux from the alloy $J_{Cr,\,Al}^{Alloy}$ at the surface is equal to or greater than the flux required to form the external oxide scale $J_{Cr,\,Al}^{Cr_2O_3,\,Al_2O_3}$, external scale formation can be sustained. This can be depicted as follows,

$$J_{Cr,\,Al}^{Alloy} \geq J_{Cr,\,Al}^{Cr_2O_3,\,Al_2O_3} \tag{7}$$

A combination of Eqs. (5) and (6) was used in the present work to evaluate the ability of an alloy to form and retain an external alumina scale in NiCrAl alloys.

Results and Discussion

General Remarks

To validate the modeling results of internal oxidation for the dilute NiCr and NiAl alloys, the experimental data from Whittle et al. [20] were utilized. The alloys studied in [20] were dilute alloys and high temperature exposures were conducted in both low partial pressures of oxygen, Ni\NiO Rhines pack and 1 atm O_2. The measured compositions of the alloys studied in [20] are given in Table 2. The grain

Table 2 Measured concentrations in wt.%. of the model alloys studied in [20] and employed in the present work for calculations

Alloy	Ni	Cr	Al
Ni-0.5Al	Bal	–	0.55
Ni-1Al	Bal	–	1.15
Ni-2.5Al	Bal	–	2.45
Ni-4Al	Bal	–	4.10
Ni-1Cr	Bal	1.1	–
Ni-2	Bal	2	–
Ni-3Cr	Bal	3	–
Ni-5Cr	Bal	4.66	–

Table 3 Measured composition of the ternary NiCrAl alloys selected in the present work from the study conducted by Giggins and Pettit [19]

Base NiCr	Ni	Cr	Al
Ni-5Cr-1Al	Bal.	5.1	1.0
Ni-5Cr-4Al	Bal.	5.0	4.0
Ni-10Cr-1Al	Bal.	10.0	1.0
Ni-10Cr-3Al	Bal.	10.0	3.1
Ni-20Cr-2Al	Bal.	19.9	2.0
Ni-20Cr-3Al	Bal.	19.9	3.0
Ni-20Cr-5Al	Bal.	19.9	4.0

size of the alloys was of the order of 350–600 µm, and the specimens were electropolished to minimize the effect of cold work. Both these factors are expected to considerably reduce the effect of grain boundaries on both inward diffusion of O and outward diffusion of alloying constituents. The depth of internal oxidation was quantified through optical metallography on etched specimens. This experimental dataset is extremely suitable for validating the results of a 1D-model which does not explicitly consider microstructural effects. Furthermore, the experimental data for exposures in Rhines pack allow a straightforward description of the boundary condition for O and eliminate the need to consider simultaneous oxidation of Ni expected to occur in the 1 atm O_2 atmosphere. For brevity, the results for the predictions of depths of internal oxidation will be limited to 1000 and 1100 °C.

The pioneering experimental work conducted by Giggins and Pettit [19] to generate oxidation maps for ternary NiCrAl alloys at 1000, 1100 and 1200 °C was utilized to validate the model predictions for minimum Al concentration required to establish an external alumina scale in NiCrAl alloys. To demonstrate the applicability of FLAP, seven ternary NiCrAl compositions were chosen from the set of test alloys studied by Giggins and Pettit [19]. The selected alloys with their compositions are given in Table 3. All of the chosen compositions lie in the single phase γ-FCC microstructure. Since all the exposures in [19] were conducted in 0.1 atm O_2, oxidation of the alloys was assumed to follow the respective thermodynamic stabilities of the pure oxides: $NiO \rightarrow Cr_2O_3 \rightarrow Al_2O_3$. The oxidation rates for the pure oxides were derived from the data for the temperature dependence of the parabolic rate constants k_p provided in Fig. 3 of [19]. The parabolic rate constant for NiO was estimated from the data for pure Ni. Since Ni-30Cr is known to form a Cr_2O_3 scale at the temperature of interest (1000 °C) [35], the corresponding values for k_p were used for Cr_2O_3. For Al_2O_3, the values for k_p given in [19] for alumina-forming alloys (Group III alloys) were utilized. For brevity, the two-step analysis of establishment and retention of the alumina scale was solely performed for the alloys studied in the present work. For the experimental data by Giggins and Pettit [19], the calculation results performed to verify the validity of Eq. (7) were omitted .

Ultimately, it is important to mention key modeling assumptions and limitations. The assumptions are as follows:

- Exclusive precipitation of pure oxides Cr_2O_3 and Al_2O_3 in the internal oxidation zone (IOZ).
- $J_O(t)$ is assumed to hold as if the oxide–alloy interface is at Ni\NiO equilibrium partial pressure
- Similar impact of precipitate shapes on transport processes in binary and ternary alloys.
- The internal oxidation behavior of Cr and Al in ternary NiCrAl alloys is similar to their respective behavior in binary NiCr and NiAl alloys
- The designation of alumina scale formation includes the formation of an alumina subscale beneath less stable oxides such as NiO and Cr_2O_3.
- Alumina scale formation was considered protective with at least 1 μm of oxide thickness (arbitrary thickness). Until this condition was established, simultaneous oxidation-induced depletion of Cr was considered.
- An average grain size of 80 μm and a grain boundary width of 0.5 nm were considered for all alloys to estimate grain boundary mobility (Eq. 4).
- Impact of Al_2O_3 precipitates on inward diffusion of O for Al concentrations > 4 wt.% similar to a Ni-4Al wt.% alloy (highest concentration evaluated by Whittle et al. [20]).

The last assumption seems justified given the reduction in the internal oxidation kinetics observed in the experimental data of [20]. At higher Al concentrations, the lateral growth of a larger fraction of Al_2O oxides might potentially negate the influence of increased interfacial O-diffusion. Some of the key limitations of the modeling approach are:

- Role of precipitate nucleation and growth are not considered
- Impact of microstructure is not explicitly considered (e.g., role of grain boundary diffusion is empirically addressed, Eq. 4)
- Influence of different precipitate shapes on transport processes is ignored
- Contribution of lateral transport and growth on scale formation is not included
- Integration of the critical volume of internal oxides (f_{IOZ}^* in Eq. 1)

Internal Oxidation Calculations for Binary NiCr and NiAl Alloys

The work of Whittle et al. [20] to evaluate the impact of dilute additions of Cr and Al on the oxygen permeation in binary NiCr and NiAl alloys was the experimental basis for the current work. Figure 1 shows the comparison between the measured and calculated depths of internal oxidation at 1000 °C and 1100 °C. There is good agreement between the two values, although the model underestimated the depth of internal oxidation for the Ni-5Cr alloy at 1100 °C. At these concentrations and high temperatures, there might be a limited impact of the oxide precipitate shape on the inward O diffusion as the kinetic data used here correspond to diffusion of O in pure Ni as given by Park and Altstetter [27]. However, the result reiterates the conclusion drawn by Whittle et al. [20] that O permeation in the dilute NiCr alloys is independent of Cr concentrations.

Fig. 1 Comparison between measured and calculated depth of internal oxidation for dilute NiCr alloys at 1000 °C. The experimental data were extracted from [20] and correspond to exposures of the alloys in Ni-NiO Rhines pack for 20 h at 1000 °C
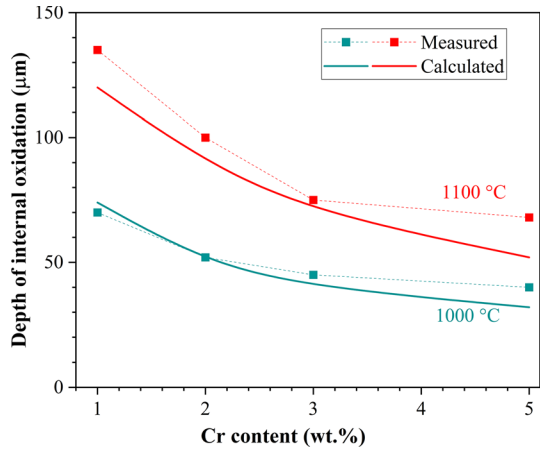

Fig. 2 Comparison between measured and calculated depth of internal oxidation for dilute NiAl alloys at 1000 °C **a** without considering enhanced O-diffusion and **b** with consideration of enhanced O-diffusion due to internal Al_2O_3 precipitates. The experimental data were extracted from [23] and correspond to exposures of the alloys in Ni-NiO Rhines pack for 20 h at 1000 °C

(a)

(b)
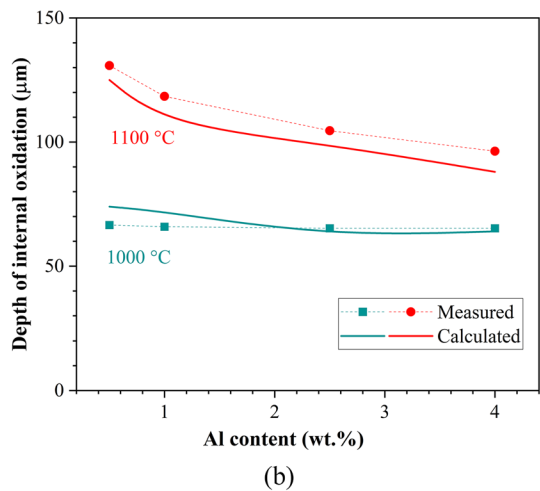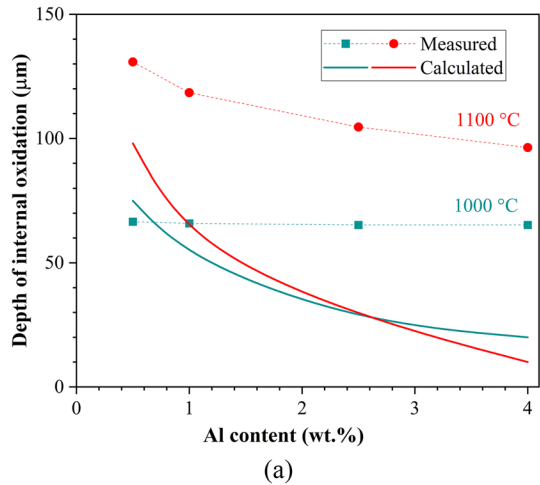
Using the same approach for the dilute NiAl alloys (Table 2), the results were less encouraging as shown in Fig. 2a. The model clearly underestimated the depth of internal oxidation at both temperatures. This result is expected due to the role of Al_2O_3 precipitates in enhancing inward O-diffusion at the oxide–matrix interfaces, as discussed by Whittle et al. [20] and Stott et al. [36], which is not considered in the 1D-model of the present work. To describe this effect, Whittle et al. [20] proposed an effective diffusion coefficient combining the O-diffusion in the Ni matrix and at the oxide–matrix interface. The approach of estimating effective diffusion coefficients is easy to implement for a binary or even a ternary system but becomes extremely challenging to extend to a multicomponent system. As was mentioned by Pillai et al. [5, 21], the use of the modified flux equation (Eq. 2) significantly reduces the computational complexity of tackling diffusion calculations in higher-order alloy systems through the use of element mobilities rather than chemical diffusion coefficients. Hence, in the present work, the O mobility at a node in the computational domain was modified when the internal oxide fraction at that location was greater than 1×10^{-4}. A satisfactory comparison of the modeling results with the experimental data after modification of O-mobilities is shown in Fig. 2b. The corresponding enhancement factors for O-mobility α_{M_O} are tabulated in Table 4. Interestingly, the modeling predictions were acceptable with the same values for α_{M_O} at both temperatures. The precise reasons for this require further analyses which are out of the scope of this work but will be part of future studies. Based on the results of Whittle et al. [20] where the ratio of the lattice diffusion of O to its diffusion at the Al_2O_3/matrix interface was similar at 900 and 1000 °C, it can be inferred that most likely the factors in Table 4 will considerably change at temperatures lower than 900 °C. It must also be mentioned here that the lattice diffusion coefficients of O in Ni employed by Whittle et al. [20] were considerably lower (2 orders of magnitude at 800 °C) than the data provided by Park and Altstetter [27].

With these results the parabolic rates of internal oxidation k_p^i were calculated for the dilute NiCr and NiAl alloys as follows,

$$\frac{\xi^2}{2t} = k_p^i \tag{8}$$

where ξ is the calculated depth of internal oxidation, and t is the time. In case of the NiCr alloys, the composition dependence of k_p^i shown in Fig. 3a was described as,

$$k_p^i = a_{Cr} e^{(-b_{Cr} C_{Cr})} \tag{9}$$

Table 4 Estimated mobility enhancement factors for O for the dilute NiAl binary alloys	Alloy	Enhancement factor at 1000 °C and 1100 °C
	Ni-0.5Al	1
	Ni-1Al	5
	Ni-2.5Al	200
	Ni-4Al	10,400

Fig. 3 Concentration dependence of the calculated parabolic rate of internal oxidation for dilute **a** NiCr and **b** NiAl alloys after exposure in Ni-NiO Rhines pack for 40 h at 900 °C, 20 h at 1000 °C and 10 h at 1100 °C
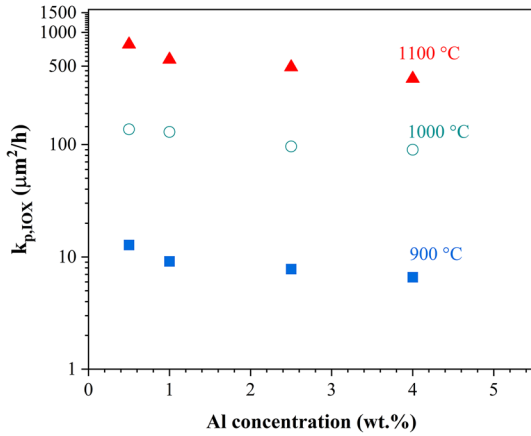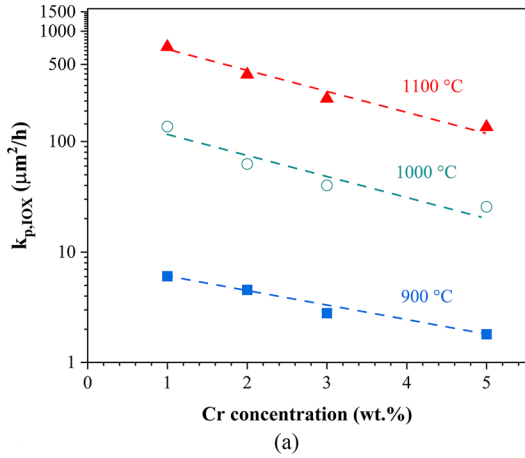

Table 5 Factors to calculate concentration dependence of the parabolic rate of internal oxidation k_p^i of Cr in binary NiCr alloys from Eq. (9)

Temperature (°C)	Factor a_{Cr} in Eq. (6) ($\mu m^2\,h^{-1}$)	Factor b_{Cr} in Eq. (6) (wt.%$^{-1}$)
900	8.1	0.31
1000	163.4	0.39
1100	972.6	0.41

The constants a and b in Eq. (9) were determined by fitting Eq. (9) to the calculated values of k_p^i and are tabulated in Table 5. The temperature dependence of a and b was described as follows,

$$a_{Cr} = a_{Cr,0} e^{\left(\frac{-A_{Cr}}{T}\right)} \quad \text{and} \quad b_{Cr} = b_{Cr,0} e^{\left(\frac{-B_{Cr}}{T}\right)} \tag{10}$$

Table 6 Factors to calculate the temperature dependence of a_{Cr} and b_{Cr} (Eq. 10) used to calculate the concentration dependence of k_p^i in Eq. (9) in binary NiCr alloys

$a_{Cr,0}(\mu m^2\ h^{-1})$	A_{Cr} (K)	$b_{Cr,0}(\mu m^2\ h^{-1})$	B_{Cr} (K)
2.2×10^{15}	38,842	2.26	2304.8

and the values for $a_{Cr,0}$, A_{Cr}, $b_{Cr,0}$ and B_{Cr} are given in Table 6. Equations (9) and (10) enable the calculation of k_p^i for different Cr concentrations and temperatures. The composition of k_p^i for the NiAl alloys shown in Fig. 3b was described using a similar approach (Eq. 9).

Fig. 4 Comparison between the measured and calculated concentration dependence of the depth of internal oxidation for dilute **a** NiCr and **b** NiAl alloys after exposure in Ni-NiO Rhines pack for 160 h at 800 °C. The error bars on the calculated values correspond to one standard deviation in the estimation of the parameters in Table 7
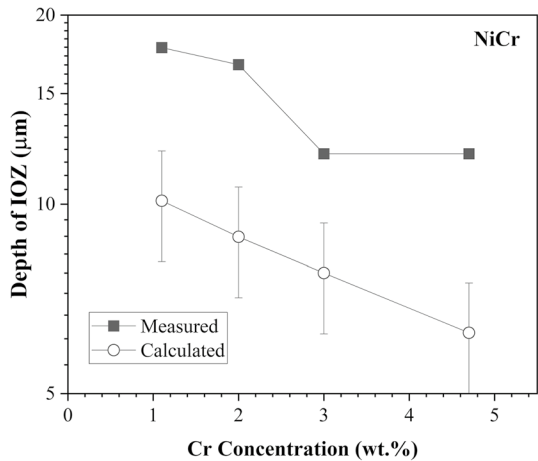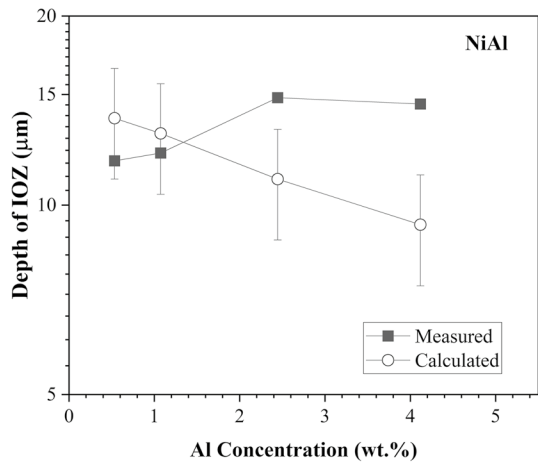
Table 7 Factors to calculate concentration dependence of the parabolic rate of internal oxidation k_p^i of Cr in binary NiAl alloys from Eq. (9)

Temperature (°C)	Factor a_{Al} in Eq. (6) ($\mu m^2\ h^{-1}$)	Factor b_{Al} in Eq. (6) (wt.%$^{-1}$)
900	12.3	0.165
1000	143.8	0.128
1100	768.8	0.177

Table 8 Factors to calculate the temperature dependence of a_{Al} and b_{Al} (Eq. 10) used to calculate the concentration dependence of k_p^i in Eq. (9) in binary NiAl alloys

$a_{Al,0}(\mu m^2\ h^{-1})$	A_{Al} (K)	$b_{Al,0}(\mu m^2\ h^{-1})$	B_{Al} (K)
5.1×10^{14}	36,782	6.5×10^{-3}	-3792.4

Using the parameters in Table 6, the depths of internal oxidation were calculated at 800 °C which is a temperature outside the dataset considered for the analyses and compared with experimental results from [20]. The comparison is shown in Fig. 4a for the depth of internal oxidation for the NiCr compositions after exposure in Ni-NiO Rhines pack for 160 h at 800 °C. The agreement is reasonable given that there were no error bars provided in the experimental data in [20].

In case of the NiAl alloys, the anomalous dependence of k_p^i on Al concentration necessitates a slightly different approach. It is evident from the experimental results in [20] that the depth of internal oxidation increased between 800 and 1000 °C but decreased at 1100 °C with increasing Al contents potentially due to the increased Al counter-diffusion at the highest temperature. With this in mind, the concentration and temperature dependence of k_p^i were derived exclusively based on the calculations at 900 and 1000 °C, under the knowledge that these are two points to demonstrate the functional relations in Eqs. (9) and (10). However, this provides an opportunity to verify the applicability of these functional forms for the experimental data at 800 °C [20], similar to the case of NiCr alloys. Figure 4b compares the measured and calculated depths of internal oxidation for the NiAl compositions after exposure in Ni-NiO Rhines pack for 160 h at 800 °C. As in the case of NiCr alloys, the model predictions agree well with the experimental data. The corresponding coefficients a_{Al}, b_{Al}, $a_{Al,0}$, A_{Al}, $b_{Al,0}$ and B_{Al} for the NiAl alloys are tabulated in Tables 7 and 8.

An additional variable that is needed to predict the minimum concentration of Cr or Al required to form an external Cr_2O_3 or Al_2O_3 scale is the maximum inward O-flux $J_{O,\ max}$ as a function of temperature and concentration. Figure 5 shows the calculated maximum surface inward O-flux for the NiCr (Fig. 5a) and NiAl (Fig. 5b) as a function of Cr and Al contents, respectively, at 900, 1000 and 1100 °C. A similar concentration and temperature dependence can be described for the O-flux given in Eq. (5). The coefficients in this case were designated as $a_{O,0}$, A_O, $b_{O,0}$ and B_O and are given in Table 9. Furthermore, the time dependence (t) of the calculated surface O-flux for a particular composition can be described as follows,

Fig. 5 Concentration dependence of the calculated maximum surface O-flux for dilute **a** NiCr and **b** NiAl alloys after exposure in Ni-NiO Rhines pack for 40 h at 900 °C, 20 h at 1000 °C and 10 h at 1100 °C
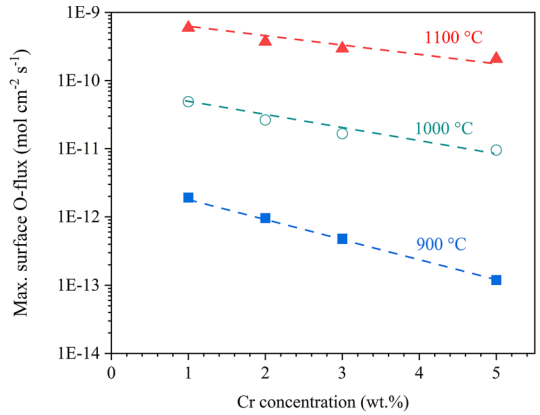

(a)
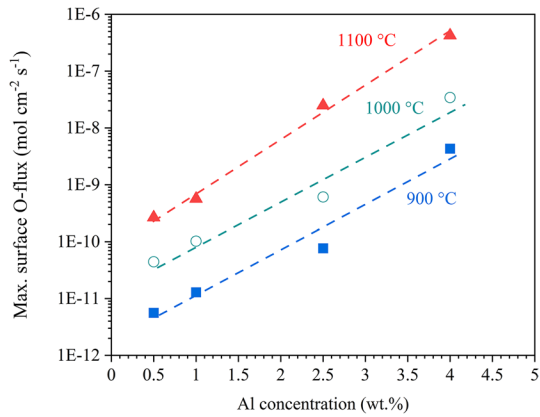
(b)

Table 9 Factors to calculate the temperature dependence of a_O and b_O (Eq. 10) used to calculate the concentration dependence of $J_{O, max}$ in Eq. (11) in binary NiCr and NiAl alloys

Alloy	$a_{O,0}$(mol cm^{-2} s^{-1})	A_O (K)	$b_{O,0}$(mol cm^{-2} s^{-1})	B_O (K)
NiCr	1.3×10^{-4}	41,957	6.3×10^{-4}	-8216.7
NiAl	5.0×10^{-9}	30,929	5.8	1346.4

$$J_O(t) = \mathrm{re}^{-\frac{t}{t'}} + s \qquad (11)$$

where r, s and t' are concentration-dependent constants by fitting the curve in to Eq. (11). $J_{O, max}$ is the value at $t \approx 0$. This function can then be implemented in the model to verify at each timestep whether Eq. (5) is satisfied. Figure 6 shows a representative plot of $J_O(t)$ for Ni-2Al and Ni-4Al alloys.

Fig. 6 Time dependence of the calculated inward surface O-flux for Ni-2Al and Ni-4Al alloys for exposures in Ni-NiO Rhines for 20 h at 1000 °C
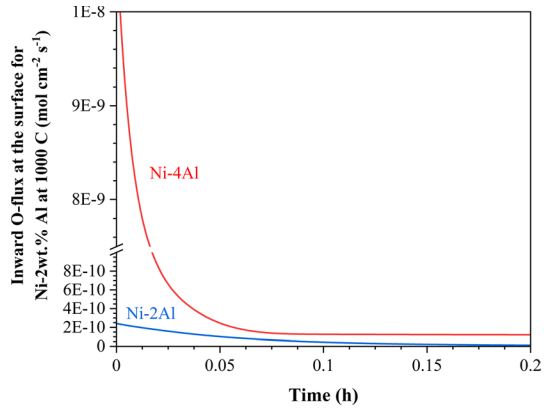
Predict Critical Concentrations for External Alumina Formation

Using the information from the previous sections on the concentration and temperature dependence of k_p^i and $J_{O,\,max}$ for the NiCr and NiAl alloys, the critical Al concentration N_{Al}^* needed to form an external alumina scale in ternary NiCrAl alloys was estimated for the compositions studied by Giggins and Pettit [19]. The experimental data generated by Giggins and Pettit were combined with the experimental results from the present work to provide adequate validation for the modeling results in the present work.

NiCrAl Alloys from Literature

Figure 7 shows the calculated ratio of outward Cr flux to inward O-flux (Fig. 7a) and outward Al flux to inward O-flux (Fig. 7b) in Ni-5Cr-1Al and Ni-5Cr-4Al alloys at 1000 °C. The boundary for external Cr_2O_3 or Al_2O_3 scale formation corresponds to the ratio 1 between the fluxes and is shown as a dotted line in the figures. In agreement with the results in [19], the Ni-5Cr-1Al is predicted to not form either an external Cr_2O_3 or Al_2O_3 scale. This alloy was shown to be a Group I (External NiO + Internal Cr- and Al-oxides) alloy. In contrast, the Ni-5Cr-4Al alloy was predicted to immediately ($t < 0.01$ h) form an external Cr_2O_3 scale followed by the formation of an external Al_2O_3 scale in about 0.1 h. The Ni-5Cr-4Al alloy was experimentally observed to be a Group III alloy (External Al_2O_3) which agrees well with model predictions.

With a higher Cr concentration of 10 wt.%, the Ni-10Cr-1Al and Ni-10Cr-3Al were both predicted to form an external Cr_2O_3 scale after 0.2 h and 0.01 h at 1000 °C, respectively (not shown here). The Ni-10Cr-1Al alloy was experimentally observed by Giggins and Pettit [19] to be at the boundary between Group I (External NiO + Internal Cr- and Al-oxides) and Group II (External Cr_2O_3 + Internal Al-oxides) alloys, indicating that local formation of a Cr_2O_3 subscale can be expected, as suggested in [19]. Formation of an external Al_2O_3 scale was only

Fig. 7 Calculated ratio of **a** outward Cr flux to inward O-flux and **b** outward Al flux to inward O-flux in Ni-5Cr-1Al and Ni-5Cr-4Al alloys at 1000 °C. The dotted line corresponds to the ratio 1 between the respective fluxes and designates the boundary for the formation of external Cr_2O_3 and Al_2O_3
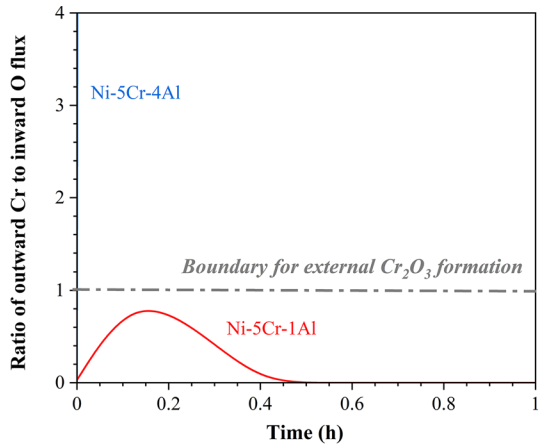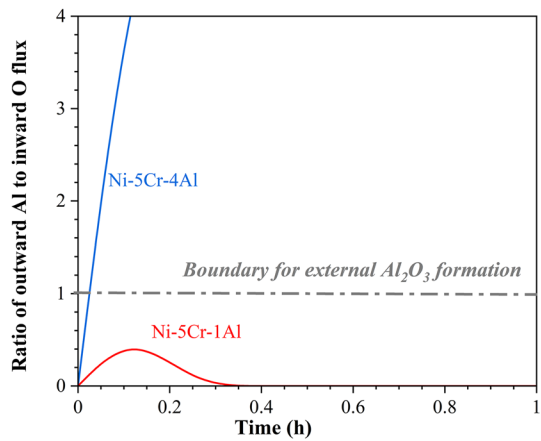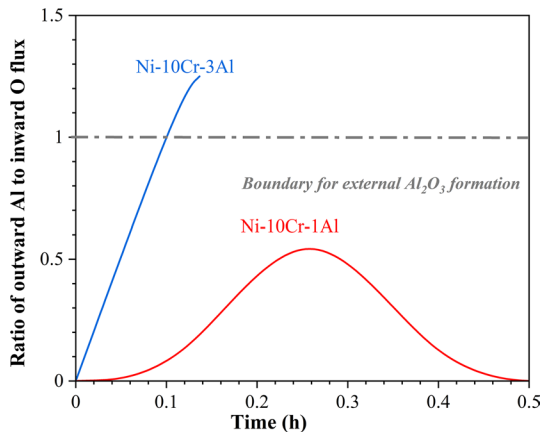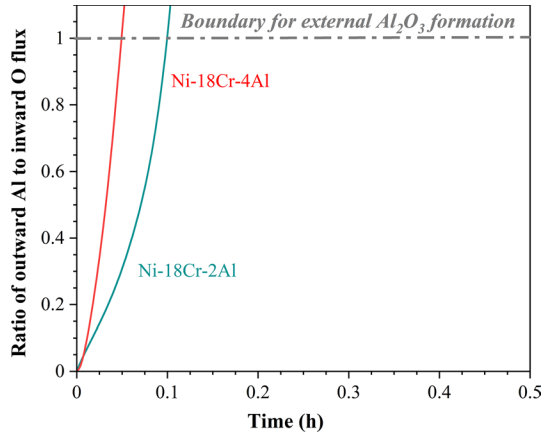
Fig. 8 Calculated ratio of outward Al flux to inward O-flux in Ni-10Cr-1Al and Ni-10Cr-3Al alloys at 1000 °C. The dotted line corresponds to the ratio 1 between the respective fluxes and designates the boundary for the formation of external Al_2O_3

Fig. 9 Calculated ratio of outward Al flux to inward O-flux in Ni-20Cr-2Al and Ni-20Cr-4Al alloys at 1000 °C. The dotted line corresponds to the ratio 1 between the respective fluxes and designates the boundary for the formation of external Al$_2$O$_3$
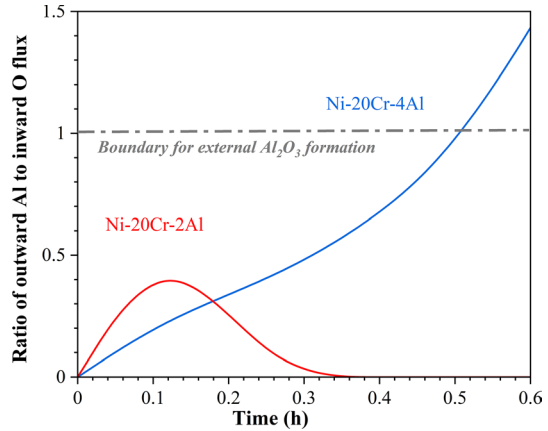
predicted for the Ni-10Cr-3Al alloy after ~0.1 h which was shown experimentally to be a Group III alloy (Fig. 8).

According to the results presented in [19], the Ni-20Cr-2Al alloy was observed to be a Group II alloy, while Ni-20Cr-3Al was a Group III alloy. The critical Al concentration for formation of an external Al$_2$O$_3$ scale in Ni-20Cr-xAl alloys was predicted to be 4 wt.% Al, as shown in Fig. 9. Al was predicted to oxidize internally in the Ni-20Cr-2Al alloy compared to the Ni-20Cr-4Al alloy which was expected to form an external Al$_2$O$_3$ scale after ~0.5 h.
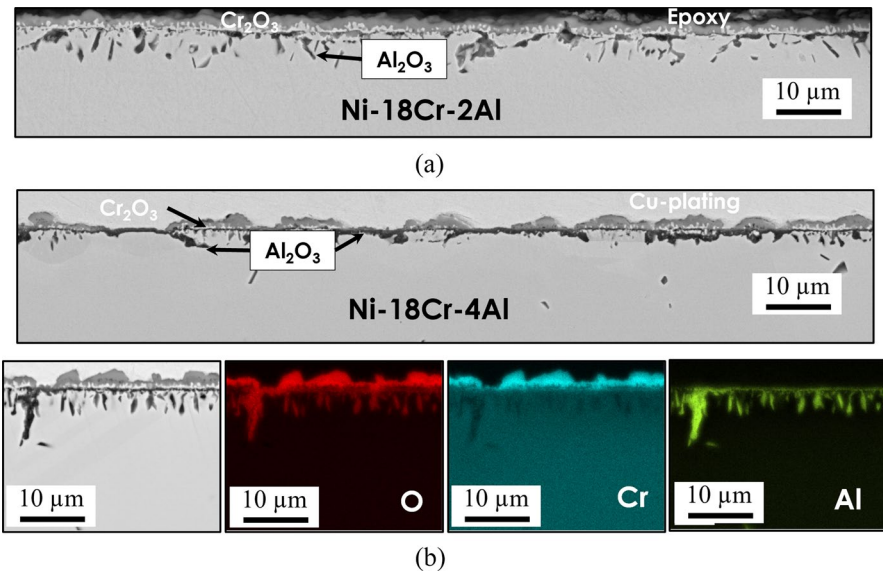
Fig. 10 **a** BSE image of the cross section of Ni-18Cr-2Al and **b** BSE image of the cross section of Ni-18Cr-4Al and corresponding elemental distribution maps (EDS) after exposure for 8 h in dry laboratory air at 950 °C

Fig. 11 Calculated ratio of outward Al flux to inward O-flux in Ni-18Cr-2Al and Ni-18Cr-4Al alloys at 950 °C. The dotted line corresponds to the ratio 1 between the respective fluxes and designates the boundary for the formation of external Al_2O_3

Fig. 12 Calculated ratio of Al-flux required to form an Al_2O_3 scale to Al-flux from the alloy at the surface in Ni-18Cr-2Al and Ni-18Cr-4Al alloys at 950 °C. The dotted line corresponds to the ratio 1 between the respective fluxes and designates the boundary for the retention of the Al_2O_3 scale
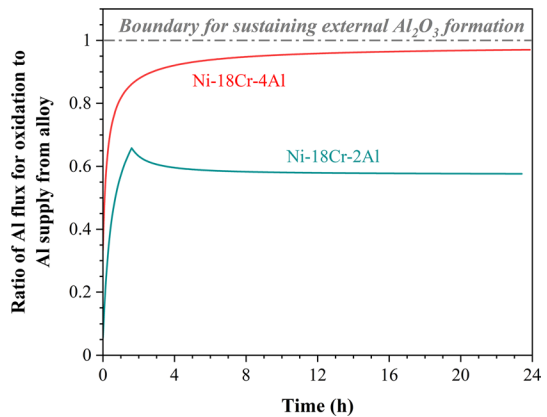
NiCrAl Alloys in the Present Work

Additional validation of FLAP was facilitated by generating experimental data for ternary NiCrAl alloys at 950 °C, a temperature outside of the temperature range studied in [19]. Figure 10 shows the BSE images of the Ni-18Cr-2Al and Ni-18Cr-4Al alloys along with the elemental distribution maps (EDS) for O, Cr and Al for Ni-18Cr-4Al after exposure in dry laboratory air at 950 °C for 8 h. Primarily, internal oxidation of Al was observed for the Ni-18Cr-2Al alloy (Fig. 10a) beneath an external Cr_2O_3 scale. However, an almost closed Al_2O_3 scale was observed at the Cr_2O_3-alloy interface in case of the Ni-18Cr-4Al alloy (Fig. 10b) accompanied by some internal Al_2O_3 precipitates, which most likely formed prior to the establishment of the Al_2O_3 subscale. The formation of an external Al_2O_3 scale was also observed at some locations. For both cases, the model predicted the establishment of an external Al_2O_3 scale (Fig. 11). However, when the potential for sustaining the formation of an external Al_2O_3 scale was evaluated, only Ni-18Cr-4Al was predicted

to retain the Al_2O_3 subscale formation (Fig. 12). Based on this result, it was concluded that the Ni-18Cr-2Al alloy will most likely internally oxidize after some local subscale formation in the initial stages. This prediction agrees with the micrograph shown in Fig. 10a. The Ni-18Cr-4Al alloy was predicted to most likely retain the initial formed alumina Al_2O_3 scale with the supply of the Al from the alloy continuously being able to support the Al consumption due to oxidation with the ratio of the fluxes being close to 1. Figure 13 compares the measured and calculated concentration profiles for Cr and Al in Ni-18Cr-4Al after exposure for 24 h in dry laboratory air at 950 °C. The good agreement between the measured and calculated values in case of Cr validates the assumption of the values of k_p for growth of chromia and the overall modeling approach.

Figure 14 shows the BSE images of the cross sections for the Ni-22Cr-1Al (Fig. 14a), Ni-22Cr-2Al (Fig. 14b), and Ni-22Cr-4Al (Fig. 14c), alloys after exposure in dry laboratory air at 950 °C for 8 h. It is evident from the images that the tendency to form an Al_2O_3 subscale beneath the external Cr_2O_3 oxide layer is the highest for the alloy with 4 wt.% Al alloy. To verify whether this would be the case, the three alloys were exposed for a longer duration of 24 h in dry laboratory air at 950 °C. The corresponding BSE images are shown in Fig. 15a, b and c. The formation of a closed and continuous Al_2O_3 subscale was observed in the Ni-22Cr-4Al alloy, while the other two alloys continued to show a mixed behavior of subscale formation and internal oxidation. The model predicted that all three alloy compositions have the potential to form an alumina subscale (Fig. 16) but Ni-22Cr-4Al alloy is the only alloy that can sustain the formation of that scale during the 24 h exposure (Fig. 17). Figure compares the measured and calculated concentration profiles for Cr (Fig. 18) and Al (Fig. 18) in Ni-22Cr-4Al after exposure for 24 h in dry laboratory air at 950 °C. Similar to the Ni-18Cr-4Al alloys, the model was able to describe the observed subsurface compositional changes indicating an adequate description of the underlying processes.

Fig. 13 Comparison between measured and calculated concentration profiles of **a** Cr and **b** Al in Ni-18Cr-4Al after exposure in dry laboratory air for 24 h at 950 °C
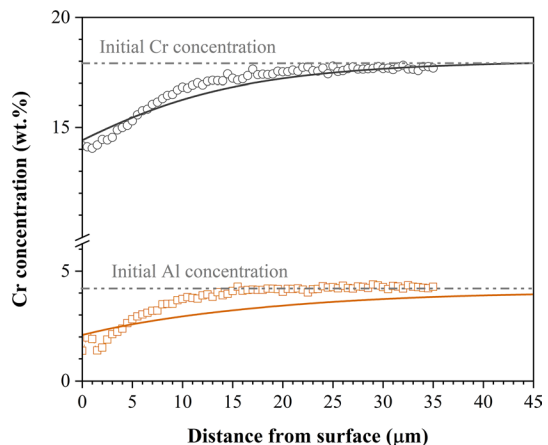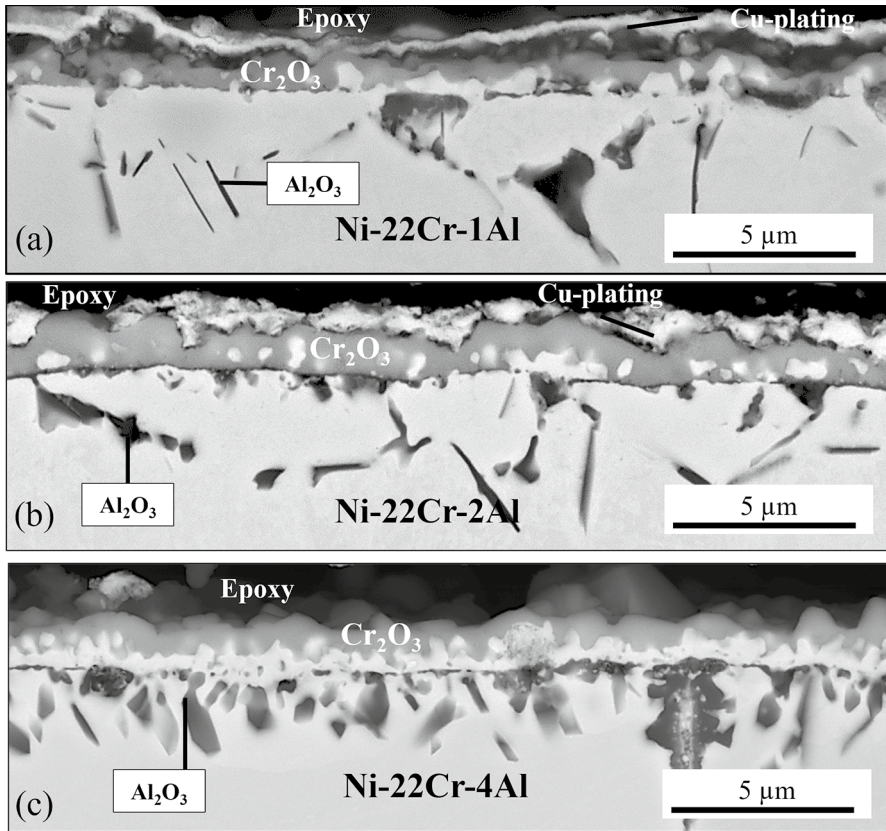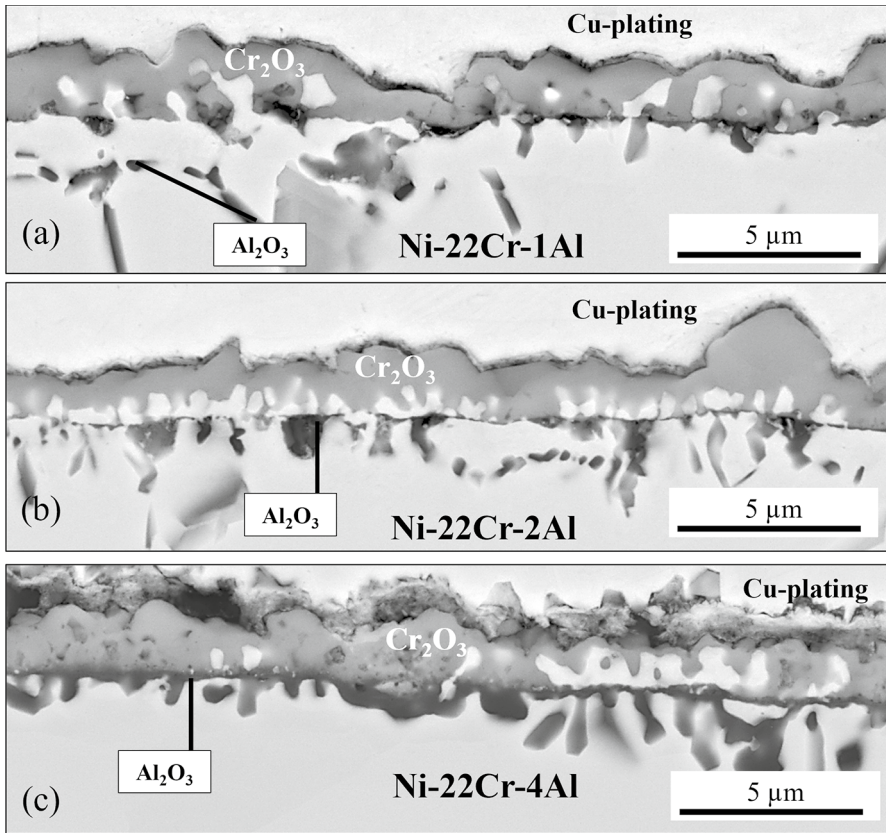
Fig. 14 **a** BSE image of the cross section of **a** Ni-22Cr-1Al, **b** Ni-22Cr-2Al and **c** Ni-22Cr-4Al after exposure for 8 h in dry laboratory air at 950 °C

Third-Element Effect

The results presented here also elucidate the "third-element effect" of Cr, which is an experimentally well-established phenomenon reported in ternary FeCrAl [37] and NiCrAl [19] alloys to reduce the minimum amount of Al needed for formation of an external Al_2O_3 scale. However, there is no unanimously accepted explanation for the underlying mechanisms for this effect and it continues to be a challenge to predict. As discussed earlier, a mere reduction in $N_O^{(s)}$ due to the formation of a Cr_2O_3 scale cannot solely predict the required Al concentrations for external scale formation. The FLAP methodology is suggesting that the likelihood of alumina scale formation in single phase γ-FCC NiCrAl alloys is significantly increased if the formation of an external Cr_2O_3 scale is possible, which is expected to happen in realistic high p_{O_2} environments. The influence of the chemical interactions between Cr and Al on the oxidation behavior and subsurface

Fig. 15 **a** BSE image of the cross section of **a** Ni-22Cr-1Al, **b** Ni-22Cr-2Al and **c** Ni-22Cr-4Al after exposure for 24 h in dry laboratory air at 950 °C

Fig. 16 Calculated ratio of outward Al flux to inward O-flux in Ni-22Cr-1Al, Ni-22Cr-2Al and Ni-22Cr-4Al alloys at 950 °C. The dotted line corresponds to the ratio 1 between the respective fluxes and designates the boundary for the formation of external Al_2O_3
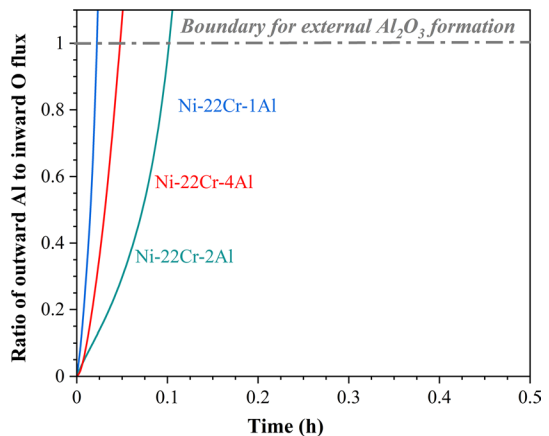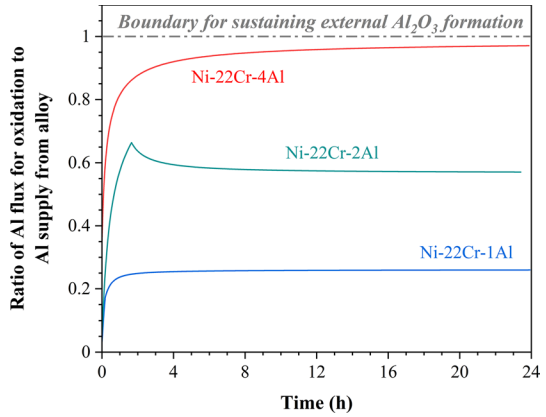
Fig. 17 Calculated ratio of Al-flux required to form an Al_2O_3 scale to Al-flux from the alloy at the surface in Ni-18Cr-2Al and Ni-18Cr-4Al alloys at 950 °C. The dotted line corresponds to the ratio 1 between the respective fluxes and designates the boundary for the retention of the Al_2O_3 scale

Fig. 18 Comparison between measured and calculated concentration profiles of **a** Cr and **b** Al in Ni-22Cr-4Al after exposure in dry laboratory air for 24 h at 950 °C
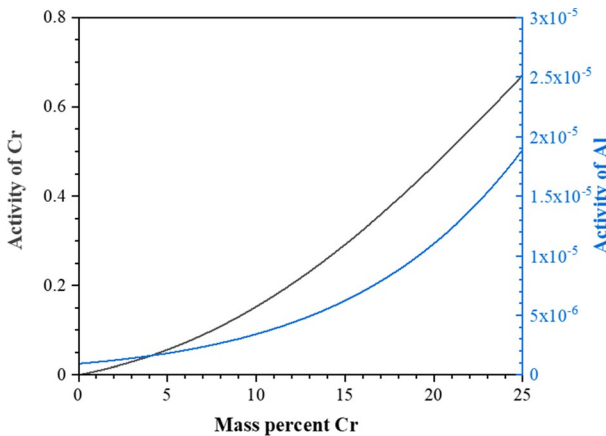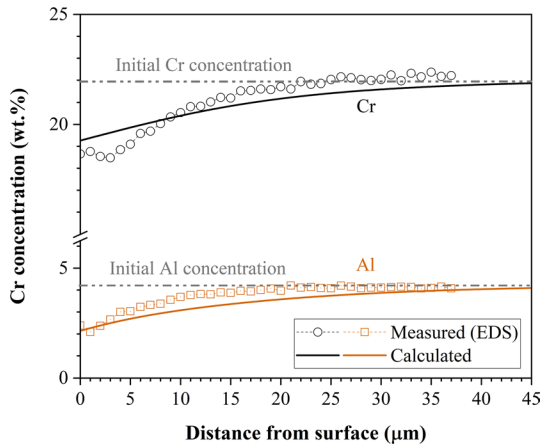
Fig. 19 Calculated [43] activities of Cr and Al with varying Cr-concentrations in a NiCr-4Al alloy at 1000 °C

compositional changes of Ni-based alloys has been discussed in the literature [10, 30, 38, 39]. The calculated chemical activities of Cr and Al demonstrate a positive interaction and this is shown in Fig. 19. A 5 wt.% change in the Cr concentration in the alloy subsurface due to oxidation nearly halves the activity of Al which can be expected to considerably increase the Al flux toward the surface and move the alloy subsurface closer toward satisfying Eq. (5). A similar approach was suggested by Nesbitt [40], but the author only accounted for the increase in Al flux due to the diffusion cross-term and its dependence on Al concentration. The role of Cr concentrations and oxidation rates was not considered.

The conclusions drawn in the present work can potentially explain why extremely high concentrations of Al (> 10–15 wt.%) are required for alumina scale formation at temperatures < 1100 °C in binary NiAl alloys [41], while Al concentrations of 3–5 wt.% generally suffice in ternary Ni–Cr–Al alloys with sufficient Cr contents (> 10 wt.%) to allow a relatively rapid formation of an external Cr_2O_3 scale [19]. At these temperatures and compositions, the binary NiAl alloys are typically multiphase with the ordered FCC and BCC phases. The formation of an alumina scale in binary NiAl alloys has to strongly rely on the nucleation of a large fraction of alumina precipitates that grow laterally to prevent internal oxidation which understandably is most likely to occur in multiphase NiAl alloys [19]. Interestingly, in the work of Giggins and Pettit [19], the alloys termed as alumina formers (Group III alloys) with Cr contents < 20 wt.% are either predominantly multiphase or contain ≥ 6 wt.% Al. In contrast, any minimal formation of an external Cr_2O_3 scale in ternary NiCrAl alloys potentially enhances the Al flux to the surface and increases the likelihood of nucleation of alumina precipitates and their eventual agglomeration supported by lateral growth. Furthermore, the drop in $N_O^{(s)}$ due to the formation of a Cr_2O_3 scale at the oxide\alloy interface aids the process by suppressing the formation of any Ni-rich oxides. This equilibrium is critical from a scale retention standpoint for the continued nucleation of alumina precipitates and their lateral growth toward formation of an alumina subscale. The continued formation of the external Cr_2O_3 scale before a closed and continuous alumina subscale can form is beneficial as it contributes to the Al flux toward the surface, as discussed earlier with reference to Fig. 19. Complementarily, the precipitation of Al_2O_3 beneath an external Cr_2O_3 layer provides an additional driving force for Cr diffusion resulting in a synergistic oxidation behavior. The latter effect of internal oxidation of Al on enhancing the Cr flux toward the surface was experimentally and computationally verified by Chyrkin et al. [39]. The role of Cr_2O_3 formation on the alloy surface in promoting nucleation of Al_2O_3 [42] cannot be ignored, but a quantitative influence of this "templating" effect in multicomponent alloys is still lacking and needs further investigations.

Conclusions

The present study demonstrated the applicability of a new modeling methodology (FLAP) to predict the minimum Al concentration required to establish and sustain an alumina scale on ternary NiCrAl alloys. The approach eliminates the limitation

of Wagner's criteria of binary single phase systems and addresses the time dependence of transport processes in the alloy subsurface. The approach is generic and can be easily extended to multicomponent-multiphase systems. The required information on the internal oxidation kinetics and inward oxygen flux was calculated independently for dilute binary NiCr and NiAl alloys. The time, concentration and temperature dependence of these values were described from the calculated data. It was assumed that the internal oxidation of Cr and Al in the ternary NiCrAl alloys progressed similar to the respective NiCr and NiAl binary alloys. Comparison of the modeling results with experimental data on the oxidation regimes for NiCrAl alloys in the literature at 1000 °C was more than satisfactory. The model was additionally able to predict well the oxidation behavior of ternary NiCrAl alloys tested in the present work at 950 °C. The results seemed to suggest that the external formation of a chromia scale is a key driver in promoting alumina scale formation underneath. The retention of the formed alumina scale is then strongly dependent on the Al content and its transport in the alloy.

Although the results are encouraging, there is a need to continue a thorough evaluation of the applicability of the approach for ternary multiphase Fe- and Ni-based alloys and even higher-order alloy systems at relevant temperatures. Advanced modeling techniques such as 2D\3D-phase field methods can aid in addressing some of the limitations in the 1D-model by accounting for lateral growth and precipitate shape. Future work will focus on addressing these aspects.

Declarations

Conflict of interest The authors declare that they have no known competing financial interests or personal relationships that could have appeared to influence the work reported in this paper.

References

1. B. A. Pint, *JOM* **65**, 1024 (2013).
2. D. Pierce, et al., *Progress in Materials Science* **103**, 109 (2019).

3. P. J. Ennis, W. J. Quadakkers, and H. Schuster, *Materials Science and Technology* **8**, 78 (1992).
4. R. Pillai, M. Romedenne and S. Lee, *Development of an Open-source Alloy selection and Lifetime Assessment Tool for Structural Components in CSP*, (United States, Medium: ED, 2022).
5. R. Pillai, A. Chyrkin, and W. J. Quadakkers, *Oxidation of Metals* **96**, 385 (2021).
6. I. G. Wright, et al., *Lifetime Modelling of High Temperature Corrosion Processes* **34**, 339 (2001).
7. D. J. Young and B. A. Pint, *Oxidation of Metals* **66**, 137 (2006).
8. W. J. Quadakkers and M. J. Bennett, *Materials Science and Technology* **10**, 126 (1994).
9. E. K. Ohriner and J. E. Morral, *Scripta Metallurgica* **13**, 7 (1979).
10. A. Chyrkin, et al., *Corrosion Science* **96**, 32 (2015).
11. R. Pillai, et al., *Corrosion Science* **127**, 27 (2017).
12. H. E. McCoy, *Oak Ridge Nat. Lab. Rev.* **3**, 35 (1969).
13. J. R. DiStefano et al., *Summary of Modified 9Cr-1Mo Steel Development Program, 1975–1985*, (United States. p. Medium: ED; Size: 301 p, 1986).
14. Y. Yamamoto, et al., *Science (New York N.Y.)* **316**, 433 (2007).
15. M. P. Brady, et al., *JOM* **60**, 12 (2008).
16. C. Wagner, *Zeitschrift für Elektrochemie, Berichte der Bunsengesellschaft für physikalische Chemie* **63**, 772 (1959).
17. J. D. Poplawsky, et al., *Scripta Materialia* **210**, 114411 (2022).
18. M. Schiek, et al., *Oxidation of Metals* **84**, 661 (2015).
19. C. S. Giggins and F. S. Pettit, *Journal of the Electrochemical Society* **118**, 1782 (1971).
20. D. P. Whittle, et al., *Philosophical Magazine A* **46**, 931 (1982).
21. R. Pillai, et al., *Materials at High Temperatures* **32**, 57 (2015).
22. R. Pillai, et al., *Calphad-Computer Coupling of Phase Diagrams and Thermochemistry* **53**, 62 (2016).
23. H. Larsson, H. Strandlund, and M. Hillert, *Acta Materialia* **54**, 945 (2006).
24. H. Larsson and A. Engstrom, *Acta Materialia* **54**, 2431 (2006).
25. Thermo-Calc, *Thermo-Calc Software TCNi8/Ni-Based Superalloys Satabase Version 8*, (Sweden, 2018).
26. MobNi5, *Thermo-Calc Software MobNi5/Ni-Alloys Mobility Database Version 5*, (Sweden, 2019).
27. J. W. Park and C. J. Altstetter, *Metallurgical Transactions A* **18**, 43 (1987).
28. A. Chyrkin et al., **96**, 32 (2015).
29. R. Pillai, et al., *Materials at High Temperatures* **35**, 78 (2017).
30. R. Pillai et al., **127**, 27 (2017).
31. R. Pillai et al., *Computational Methods to Accelerate Development of Corrosion Resistant Coatings for Industrial Gas Turbines*. (Superalloys, 2020).
32. R. Pillai, S.S. Raiman and B.A. Pint, *Journal of Nuclear Materials*, **546**, 152755 (2021).
33. R. Pillai, et al., *JOM* **75**, 994 (2023).
34. C. Wagner, *Journal of the Electrochemical Society* **99**, 369 (1952).
35. C. S. Giggins and F. S. Pettit, *Transactions of the Metallurgical Society of Aime* **245**, 2495 (1969).
36. F. H. Stott, et al., *Solid State Ionics* **12**, 365 (1984).
37. P. Tomaszewicz and G. R. Wallwork, *Oxidation of Metals* **20**, 75 (1983).
38. A. Chyrkin, et al., *Corrosion Science* **124**, 138 (2017).
39. A. Chyrkin, et al., *Materials at High Temperatures* **32**, 102 (2015).
40. J. A. Nesbitt, *Journal of the Electrochemical Society* **136**, 1511 (1989).
41. F. S. Pettit, *Transactions of the Metallurgical Society of Aime* **239**, 1296 (1967).
42. R. Klumpes, et al., *Werkstoffe Und Korrosion-Materials and Corrosion* **47**, 619 (1996).
43. Thermo-Calc, *Thermo-Calc Software TCNi11/Ni-Alloys Database Version 11.0*, (2021).